Theoretical and Applied Fracture Mechanics 124 (2023) 103803

Contents lists available at ScienceDirect

Theoretical and Applied Fracture Mechanics

journal homepage: www.elsevier.com/locate/tafmec

On the experimental characterisation of crack tip displacement fields on nonplanar elements: Numerical and experimental analysis

A. Camacho-Reyes [a,*], F.V. Antunes [b], J.M. Vasco-Olmo [a], F.A. Diaz [a], L.A. Felipe-Sesé [a]

[a] Departamento de Ingeniería Mecánica y Minera, Universidad de Jaén, Jaén, Spain
[b] Univ Coimbra, Centre for Mechanical Engineering, Materials and Processes (CEMMPRE), Department of Mechanical Engineering, Portugal

ARTICLE INFO

Keywords:
Crack tip field
Non-planar surface
Curved circumferential crack
3D-DIC
FEA
AISI 304L

ABSTRACT

In this work, a numerical and experimental study about crack tip fields characterisation on curve-cracked elements has been performed. This study combines a novel differential geometry approach combined with 3D-DIC and FEA results to determine crack-tip parameters from the displacement field on a curved cracked element. The work aims to validate and compare some aspects that cannot be addressed using 3D-DIC. SIFs for different crack lengths are determined using DIC and FEA data and compared In addition, a comprehensive comparison between experimental and numerical fields is done using an Image Decomposition technique based on Tchebichef polynomials.

1. Introduction

In the last decades, the development of full-field optical techniques for the measurement of stresses, strains or displacements [1–3] has allowed addressing fatigue and fracture problems to clarify some either unresolved or at least unclear issues. In particular, the combination of experimentally measured crack tip fields together with the analytical description of the crack tip fields [4–10] has contributed to a better understanding of the effective fatigue crack driving forces for fatigue advance [11–13], to assess the influence of the plastic zone during fatigue crack propagation [14,15] as well as the determination of the crack tip singularity parameters [16,17] among others.

One of the major limitations of the above-mentioned crack tip field models' lies in their applicability to only flat surfaces under plane stress or strain considerations. In the literature, some works [18–23] can be found where 2D or 3D optical techniques for stress and strain measurement are employed in combination with analytical crack tip fields models to infer singularity parameters in cracked curved shape elements. However, in all the cases the surface is assumed as flat which may lead to significant errors in the experimental calculation of crack tip parameters such as the stress intensity factor, the crack tip opening displacement or the plastic zone size. Such an example is the work conducted by Vormwald *et al.* [23]. They inferred mixed-mode stress intensity factors from 3D-DIC data on a thin-walled cylindrical pipe using a 2D crack tip field model by assuming a hypothetical negligible curvature with very high magnification. Mokhtarishirazabad *et al.* [22] employed 2D-DIC with a high magnification lens to determine stress intensity factors on a cylindrical cracked surface using the Williams crack tip field model [6]. Although the results reported by the above-mentioned authors present a good agreement with results obtained by other methods, some inconveniences could be found when the negligible curvature hypothesis is used. The first, and maybe the most important inconvenience, is the existence of a plastic enclave near the crack tip because when a high magnification lens is employed there is a risk of partial or total inclusion of plastic data in fitting data. To avoid plastic data inclusion, a wider field of view is required which imply to reduce the spatial resolution and hence, to analyse a zone where the curvature effect is not negligible. Secondly, displacement field directions cannot be modelled correctly since crack growth direction is assumed as a straight line and in consequence, the displacement field components considered for fitting do not correspond to real crack-open and the crack-growth directions considered in any crack tip field mathematical formulation.

To address this issue avoiding above described inconveniences, some authors of the present paper developed a differential geometry-based approach to characterise the crack tip displacement field on a nonplanar and developable surface under plane stress consideration [24]. This approach, previously validated experimentally, supposes an important advance in the field of experimental fracture mechanics and its implications for fatigue. This method allows for assessing curved-fractured elements from a theoretical–experimental approach that does not require additional validations due to its nature. In addition, the

* Corresponding author.
E-mail address: acreyes@ujaen.es (A. Camacho-Reyes).

https://doi.org/10.1016/j.tafmec.2023.103803
Received 4 November 2022; Received in revised form 31 December 2022; Accepted 31 January 2023
Available online 4 February 2023

Nomenclature

u_x, u_y, u_z	Displacement field components in a Cartesian system
r, θ	Polar coordinates
G	Shear modulus
ν	Poisson' coefficient
κ	Function depending on Poisson's coefficient
K_I	Opening mode stress intensity factor
σ_{0x}, σ_{0y}	Non-singular stresses along crack growth and opening directions
a_p	Coefficient number p of the Williams' series
p	Sum index
x, y, z	Cartesian coordinates
$\sigma_x, \sigma_y, \tau_{xy}$	Plane stress tensor components
ξ, η	Parametrisation parameters
$\overrightarrow{\rho}$	Position vector
$\overrightarrow{T}, \overrightarrow{B}, \overrightarrow{N}$	Frenet-Serret trihedron components
$\overrightarrow{e_x}, \overrightarrow{e_y}, \overrightarrow{e_z}$	Unitary vectors along Cartesian directions
x', y'	Coordinates on the unwrapped plane
ξ_0, η_0	Lower integration limits for curve lengths determination
u_T, u_B, u_N	Displacement field components along Frenet directions
r', θ'	Polar coordinates on the unwrapped plane
z_n	Normal coordinate to unwrapped plane
σ_T, σ_B	Stress components along Frenet directions
$I(i,j)$	Image decomposition intensity matrix
f_i	Intensity of each Tchebichef moment
$\widetilde{T}_i(i,j)$	Normalised shape descriptor
$\boldsymbol{\sigma}'$	Deviatory Cauchy stress tensor
$\boldsymbol{X}$	Back-stress tensor
Y	Flow stress
σ_0, Q, b	Voce law parameters
$\overline{\varepsilon}$	Equivalent plastic strain
C, D	Material elastoplastic behaviour parameters
$\dot{X}$	Back stress rate
F^{exp}	Error function for experimental displacement field fitting
F^{num}_{disp}	Error function for numerical stress fitting
F^{num}_{stress}	Error function for numerical displacement fitting
P	Axial load
R	Cylindrical pipe mean radius
t	Cylindrical pipe wall thickness
γ	Crack angle
r_c, θ_c, z_c	Cylindrical coordinates on the cylinder system

proposed approach can assess some complex geometry problems that can be solved only numerically thus far. In the previous work [24], that methodology is experimentally validated through the analysis of mode I SIFs on hollow cylinders containing circumferential cracks as well as comparing the mathematically modelled and experimentally measured surrounding crack tip displacement fields for different crack lengths.

The present work combines FEA and DIC data to perform a deep analysis addressing not only a single characterising parameter as K but establishing a full-field comparison between experimental and numerical crack tip displacement fields through a Tchebichef polynomials-based image comparison technique [25–27]. The inclusion of FEA data is one of the keys for a comprehensive validation beyond the comparison between both data, since FEA allows through-thickness information to be obtained for full stress tensor determination. Thus, the plane stress hypothesis can be directly verified in contrast to 3D-DIC analysis, which allows only on the surface information to be measured and hence, providing an indirect validation way.

2. Fundamentals

2.1. Williams' crack tip field model

According to Williams [6], the crack tip displacement field under plane stress or plane strain conditions is described as a expansion series governed by different coefficients, which are related to each expansion series term, in function of the polar coordinates in the crack plane. The displacement field at the surroundings of the crack tip under pure fracture mode I is given by equation (1).

$$\left\{\begin{array}{c} u_x \\ u_y \end{array}\right\} = \sum_{p=1}^{\infty} \frac{r^{\frac{p}{2}}}{2G} a_p \left\{\begin{array}{c} \left(\kappa + \frac{p}{2} + (-1)^p\right)\cos\frac{p\theta}{2} - \frac{p}{2}\cos\frac{(p-4)\theta}{2} \\ \left(\kappa - \frac{p}{2} - (-1)^p\right)\sin\frac{p\theta}{2} + \frac{p}{2}\sin\frac{(p-4)\theta}{2} \end{array}\right\} \quad (1)$$

Where u_x and u_y are the displacement field components, r and θ are a set of polar coordinates over the crack plane referred to the crack tip (Fig. 1), G is the shear modulus, κ is $(3-\nu)/(1+\nu)$ for plane stress conditions, ν is Poisson's coefficient, p is a sum index and a_p is the p_{th} series coefficient. The first coefficient is related to mode I stress intensity factor ($K_I = \sqrt{2\pi}a_1$) and the second coefficient is related to T-stress ($T_x = 4a_2$).

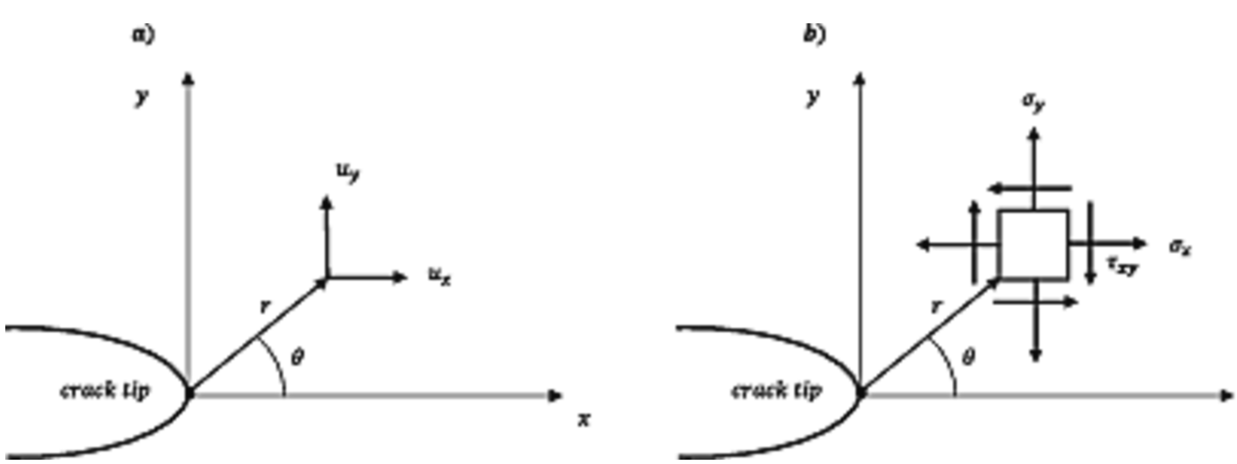

Fig. 1. Schematic representation showing (a) the displacement field components and (b) the stress tensor at a point near the crack tip defined by coordinates (r,θ).

The displacement component normal to the crack plane is given by:

$$u_z = -2z\frac{G(1+\nu)}{\nu}(\sigma_x+\sigma_y) \tag{2}$$

In this expression σ_x and σ_y are the normal stresses and z is the coordinate normal to the crack plane. The stress tensor components at the surrounding of the crack tip are given by:

$$\left\{\begin{array}{c}\sigma_x\\ \sigma_y\\ \tau_{xy}\end{array}\right\} = \sum_{p=1}^{\infty}\frac{p}{2}a_p r^{\frac{p-2}{2}}\left\{\begin{array}{c}\left(2+(-1)^p+\frac{p}{2}\right)\cos\left(\frac{p}{2}-1\right)\theta-\left(\frac{p}{2}-1\right)\cos\left(\frac{p}{2}-3\right)\theta\\ \left(2-(-1)^p-\frac{p}{2}\right)\cos\left(\frac{p}{2}-1\right)\theta+\left(\frac{p}{2}-1\right)\cos\left(\frac{p}{2}-3\right)\theta\\ -\left((-1)^p+\frac{p}{2}\right)\sin\left(\frac{p}{2}-1\right)\theta+\left(\frac{p}{2}-1\right)\sin\left(\frac{p}{2}-3\right)\theta\end{array}\right\} \tag{3}$$

where τ_{xy} is the shear stress in the crack plane. By convention, the x-axis corresponds to the crack-growth direction and the y-axis represents the crack-opening direction under tensile loading, as illustrated in Fig. 1:

2.2. Extended crack tip model for the analysis of curved surfaces

This differential geometry-based approach reported in [24] consist of introducing some geometrical modifications in original flat crack tip field models in order to characterise the surrounding crack tip displacement field on a non-planar and developable surface under plane stress conditions. Let an orthogonal and developable surface which contains a crack growing in a direction ξ and where the crack opening directions is characterized through a direction η, orthonormal to ξ and contained in the crack plane. If a plane stress state exists such that there are no stress components outside the surface containing the crack, an analogy with planar crack tip field models can be established by replacing the original crack growth and opening directions by the curve crack growth and opening directions and the original linear coordinates by a set of curve coordinates corresponding to those curve directions (see Fig. 2).

Thus, the previously described geometrical modifications lead to rewrite a flat 2D crack tip field model (Williams' series model for opening pure fracture mode I is used here) as shown below:

$$\left\{\begin{array}{c}u_T\\ u_B\end{array}\right\} = \sum_{p=1}^{\infty}\frac{r'^{\frac{p}{2}}}{2G}a_p\left\{\begin{array}{c}\left(\kappa+\frac{p}{2}+(-1)^p\right)\cos\frac{p\theta'}{2}-\frac{p}{2}\cos\frac{(p-4)\theta'}{2}\\ \left(\kappa-\frac{p}{2}-(-1)^p\right)\sin\frac{p\theta'}{2}+\frac{p}{2}\sin\frac{(p-4)\theta'}{2}\end{array}\right\} \tag{4}$$

In this expression, u_T and u_B are the components of the displacement field on the unwrapped plane and r' and θ' are a set of polar coordinates referred to the crack tip over the unwrapped plane whose equivalent Cartesian coordinates are x' and y'. As shown in Fig. 2, u_T corresponds to the displacement along the crack growth direction (parametrisation direction ξ) and u_B corresponds to the crack opening direction (parametrisation direction η). These new components are obtained by projecting the Cartesian displacement field over Frenet-Serret unitary directions [28], which are obtained through the position vector and each parametrisation direction, on each point of the surface. Frenet-Serret unity vectors are given by the following equations

$$\overrightarrow{T} = \frac{\frac{\partial\overrightarrow{\rho}}{\partial\xi}}{\left\|\frac{\partial\overrightarrow{\rho}}{\partial\xi}\right\|} \tag{5}$$

$$\overrightarrow{B} = \frac{\frac{\partial\overrightarrow{\rho}}{\partial\eta}}{\left\|\frac{\partial\overrightarrow{\rho}}{\partial\eta}\right\|} \tag{6}$$

$$\overrightarrow{N} = \overrightarrow{T}\times\overrightarrow{B} \tag{7}$$

where $\overrightarrow{T}$, $\overrightarrow{B}$ and $\overrightarrow{N}$ are the tangential, binormal and normal unity vectors that compound the Frenet-Serret trihedral and $\overrightarrow{\rho}$ is a position vector referred to an arbitrary coordinate system. In this expression, double vertical bars denote the module of the vector and $\times$ the vector cross product. The lengths x' and y' over the surface along the parametrisation directions, ξ and η, are obtained by integration according to:

$$x' = \int_{\xi_0}^{\xi}\left\|\frac{\partial\overrightarrow{\rho}}{\partial\xi}\right\|d\xi \tag{8}$$

$$y' = \int_{\eta_0}^{\eta}\left\|\frac{\partial\overrightarrow{\rho}}{\partial\eta}\right\|d\eta \tag{9}$$

Here, ξ_0 and η_0 are lower integration limits.

2.3. Image decomposition technique

Image decomposition has been employed for the evaluation of the agreement between the displacement maps obtained experimentally and by FEA.

This procedure consists of decomposing each displacement map into a multidimensional vector of Shape Descriptors. These descriptors are independent from scale or orientation of the original displacement maps. Hence as pointed by previous authors and protocols [25,29,30], it is an interesting procedure for the comparison of results obtained from different techniques such as those obtained experimentally and numerically as considered in this work. In fact, this method is widely employed for validation of analytical and theoretical models [29]. One interesting aspect is the fact that feature vectors obtained by different

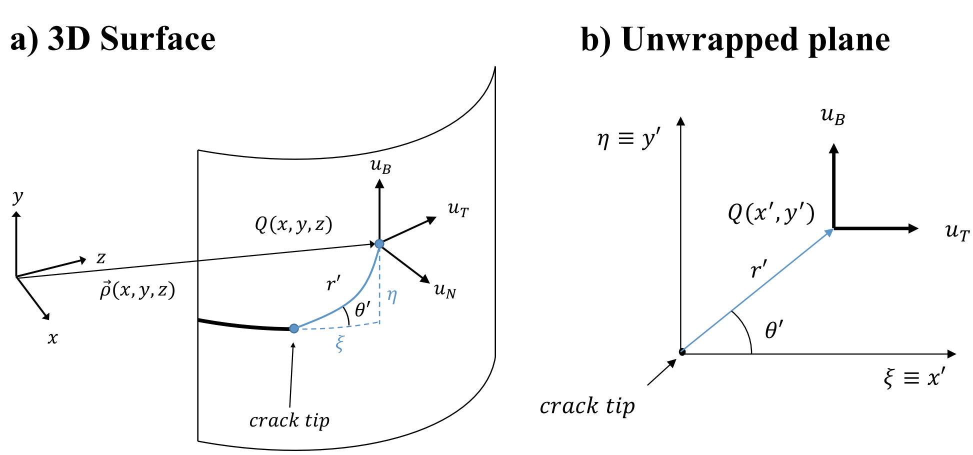

Fig. 2. Illustration to stablish the analogy with flat models. Cracked surface (a) and the equivalent system on the unwrapped plane (b).

techniques can be compared directly, for instance computing the correlation coefficient between them or even the Euclidean distance between vectors. This distance can be considered as the difference between maps in the same units as the original data fields.

In this work, each displacement map obtained experimentally and numerically for each crack length has been decomposed and compared. The displacement maps, considered as a matrix of intensity I*(i,j)*, have been decomposed in Tchebichef polynomials $\widetilde{T}(i,j)$ [30–32]:.

$$I(i,j) = \sum_{i=1}^{N} f_i \widetilde{T}_i(i,j) \tag{10}$$

f_i is the intensity of the ith Tchebichef moment and the normalised shape of the descriptor is $\widetilde{T}_i$. N is the number of shape descriptors in which the data field is decomposed. More information about the decomposition procedure could be found in the work performed by Wang *et al.* [32]. The required number of shape descriptors is given by the achievement of a proper correlation coefficient between the original and the reconstructed image using N shape descriptors [33].

3. Experimental details

To support and validate the above exposed methodology, a fatigue crack growth test was carried out on a round thin wall pipe made of 304L austenitic stainless steel. The chemical composition and the mechanical properties are displayed in Tables 1 and 2, respectively. The specimen was designed according to ASTM standard E-606–92 [34]. Specimen dimensions are 203.2 × 26.7 × 2.11 mm (length × diameter × thickness). To a correct gripping during the test, cylinder ends were machined to 25.4 mm (outer pipe diameter) being the machined length 50.8 mm at each end (axial distance from the end of the specimen). A notch was introduced at the specimen centre by drilling a 1.5 mm through-thickness hole and introducing 0.1 mm circumferential sawn slots. Fig. 3 shows a specimen drawing and the manufactured specimen together with a schematic notch view. The notch length (hole + slot) is around 2 % of the outer circumference perimeter. This small length was chosen to avoid the effect of the manufacturing process residual stresses that might affect to the singularity crack tip field. Thus, as the crack grows (higher crack lengths than the initial notch length) the residual stresses effect on crack tip fields should be disappear and hence its influence on crack tip singularity parameters. Fatigue test was carried out in a 100 kN servohydraulic testing machine model MTS Landmark 370.10. A constant amplitude cyclic load was applied at the frequency of 10 Hz. The stress ratio was 0.525 to avoid possible crack closure influences on the fatigue crack growth rate [35]. The maximum load was chosen to be significantly higher than the threshold value in order to induce fatigue crack growth [35]. Hence, as maximum load, 30 % of the load equivalent to the yield stress was chosen (maximum and minimum loads 20 and 10.5 kN). Fig. 4 shows a schematic representation of the crack growth shape (Fig. 4a) and a plain view of the fractured surface after fatigue test (Fig. 4b).

For a correct DIC processing, the specimen surface was painted with a stochastic black speckle on a white background. To record the 3D crack tip displacement field, a stereoscopic vision system comprising three 5-megapixel monochrome CCD cameras was used. To increase the spatial resolution surrounding the crack tip, each camera was fitted with a macro-zoom lens (MLH-10X EO). The curve nature of the surface requires a greater deep of field to avoid a blurring effect. Hence, a small lens aperture was set. A smaller lens aperture imply that camera sensor receives low light. Thus, to achieve a uniform illumination on both sides of the specimen, a dual-point optic fibre light guide was employed. As the imaging process was performed at a low frequency, the integration time was not a significant variable and it was chosen in order to achieve good illumination during the imaging stage. The experimental set-up for fatigue test is shown in Fig. 5

Table 1
Mass chemical composition of 304L stainless steel.

Element	C	Si	Mn	S	P	Ni	Cr
(%wt)	0.02	0.39	1.37	0.001	0.029	8.01	18.15

Table 2
Mechanical properties of 304L-SS.

Mechanical property	Units	Value
Elastic modulus	GPa	197
Poisson's coefficient	–	0.33
Yield stress (0 %)	MPa	117
Yield stress (0.2 %)	MPa	220
Tensile strength	MPa	646
Elongation at failure	%	53

The stereoscopic system geometric calibration was done utilising a calibration grid that was generated using the software Target Generator provided by Correlated Solutions Inc. [36]. The calibration grid consist of a rectangle comprising 9 × 6 dots evenly spaced 2 mm apart. The average spatial resolution achieved was 0.02 mm/pixel. For DIC processing, vIC-3D software provided by Correlated Solutions Inc. was employed [36]. A subset facet size of 29 pixels and a step/overlap of one pixel were employed.

4. Numerical modelling

ABAQUS software was employed to replicate the experimental test accounting for geometry, loading and the material properties. The symmetry of the problem (double symmetry relatively to two planes radial-tangential and axial-radial) allows the model to be simplified through modelling only a quarter of the specimen. Furthermore, cylinder ends were not included since they do not affect to results in terms of surrounding crack tip fields. In addition, the specimen notches (through-thickness holes + sawn slots) were removed for two reasons. First, the notch geometry effect does not modify the simulated fields since the simulated crack lengths are higher than the initial notch (around 1 degree in terms of the subtended angle by the crack). That is, the hole can be considered as an initial notch. Secondly, possible existing residual stresses due to the notch manufacturing process does not affect the crack tip singularity parameters for crack lengths higher than the initial notch length (see Section 6). Fig. 6a shows the numerically modelled geometry. As shown in Fig. 6b, 6c and 6d, symmetry conditions were modelled through constraining normal displacements to symmetry planes of the geometry. Saint-Venant principle allows the applied axial loading to be modelled as uniform loading at the top of the model (see Fig. 6c). Thus, this remote stress was calculated as the ratio between the applied axial loading and the annulus area. A sinusoidal function was employed to model overtime load variation at the frequency of 10 Hz. The same conditions were chosen as for the experimental test in terms of maximum load and stress ratio (maximum load 30 % of the yield stress and stress ratio of 0.525). Authors note that the input frequency was established only to generate a time domain since no transient effects were included in the numerical model. Cracks were modelled by eliminating symmetry conditions at the bottom of the model (green area in Fig. 6).

The elastic behaviour was modelled using generalised Hooke's law. The plastic behaviour was modelled via the Von Mises criterion along with a combined kinematic-isotropic hardening model. The von Mises yield surface is given by equation (11):

$$\sqrt{\frac{3}{2}(\boldsymbol{\sigma}' - \boldsymbol{X}) : (\boldsymbol{\sigma}' - \boldsymbol{X})} - Y \leq 0 \tag{11}$$

Where $\boldsymbol{\sigma}'$ represents the deviatory Cauchy stress tensor, $\boldsymbol{X}$ is the back-stress tensor and Y is the flow stress. The combined evolution of Y and $\boldsymbol{X}$ with plastic deformation is described by Voce isotropic [37] and

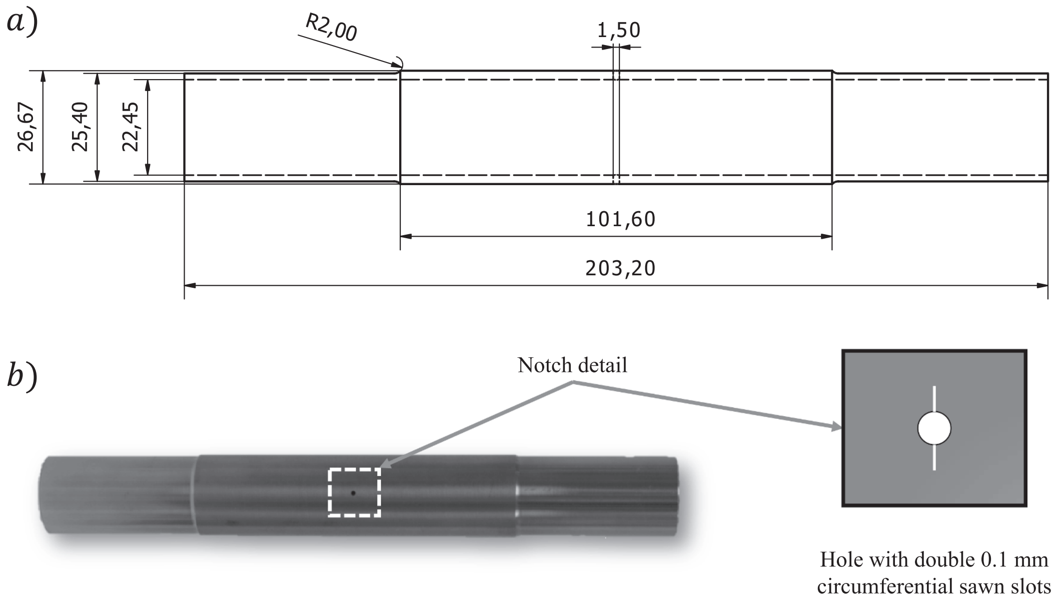

Fig. 3. 304L-SS specimen used during fatigue test. (a) Specimen drawing and (b) manufactured specimen showing a notch detail.

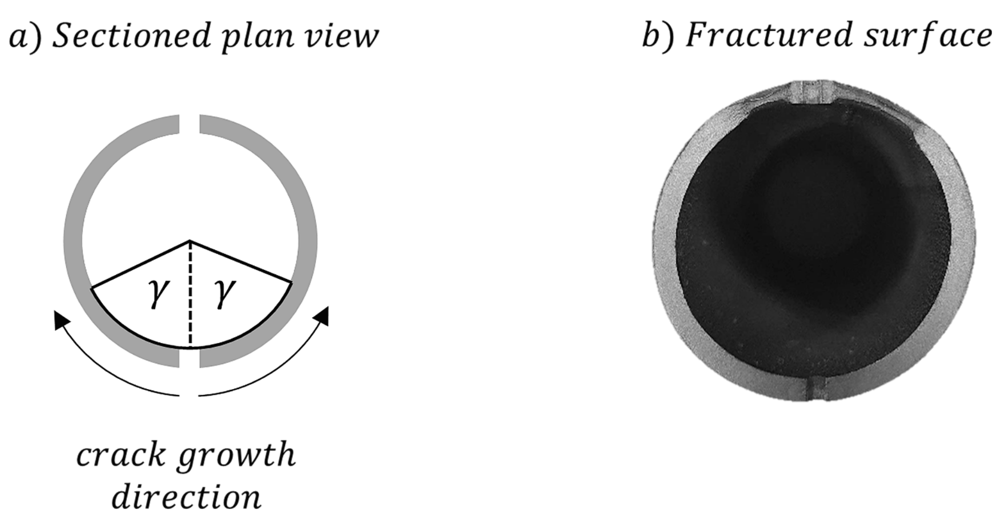

Fig. 4. (a) Schematic view showing crack growth shape and crack angle definition and (b) specimen fractured surface due to fatigue test.

Chaboche kinematic hardening laws [38] according to equations (12) and (13):

$$Y = \sigma_0 + Q[1 - \exp(-b\bar{\varepsilon})] \tag{12}$$

$$\dot{X} = \frac{2}{3}C\dot{\varepsilon} - DX\dot{\bar{\varepsilon}} \tag{13}$$

Where σ_0, Q and b are material parameters of the Voce law, $\bar{\varepsilon}$ is the equivalent plastic strain; C and D are material parameters of the Chaboche law, $\dot{X}$ is the back-stress rate, $\dot{\varepsilon}$ and $\dot{\bar{\varepsilon}}$ are respectively the plastic strain rate and the equivalent plastic strain rate. In the case of uniaxial cyclic loading, integration of equation (13) gives:

$$X = \chi C + (X_0 - \chi C)\exp(-\chi D(\varepsilon - \varepsilon_0)) \tag{14}$$

Where X_0 and ε_0 are the values of X and ε at the beginning of each half cycle, where $\chi = \pm 1$ during loading and unloading, respectively. Material parameters were obtained fitting the model to cyclic stress–-strain loops obtained in low-cycle fatigue tests [39]. Materials parameters are shown in Table 3.

The computational domain was discretised using 3D quadratic hexahedral elements (C3D20). Computational cost was reduced by generating two regions (refined and coarse zones) as shown in Fig. 7. To avoid mesh transitions which may lead to mesh distortions and therefore, inaccurate results, both parts were "tied" using a displacement constraint consisting of imposing the same displacement at the boundaries of the connected zones. The refined zone at the model bottom consists of a ¼ of a cylinder with a height of 25 % of the cylinder half-height. This height was previously determined in order to capture enough singularity data for the larger simulated crack lengths. In addition, the size of the finite elements used in the refined zone was 0.1 × 0.1 × 0.21 mm^3 (length × height × depth). Although lower element sizes have been used in literature [40,41], for the purpose of the present work this size was enough since plastic zones were properly reproduced for the crack lengths analysed. Thus, in the refined zone the total number of elements and nodes were 258,690 and 1,112,367 nodes, respectively. The coarse zone was modelled employing 11,180 nodes and 285 elements with a size of 2.2 × 2.2 × 2.1 mm^3.

To model cracks using FEA, many approaches can be found in the literature such as based on singular element [42], cohesive elements [43] or phase-field models [44,45] among others. However, in this work, the

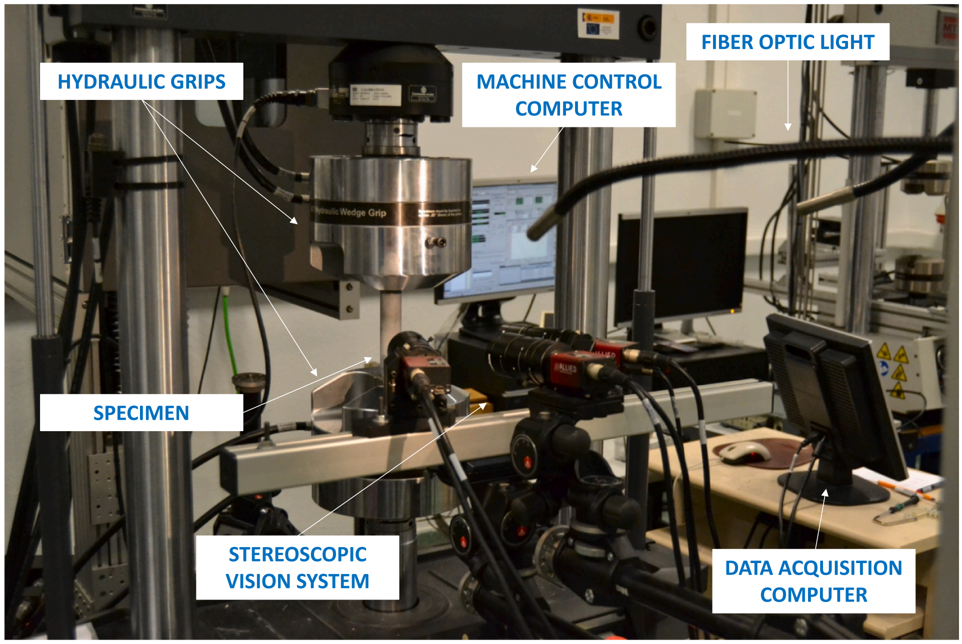

Fig. 5. Set-up for acquiring 3D crack tip displacement fields during fatigue testing.

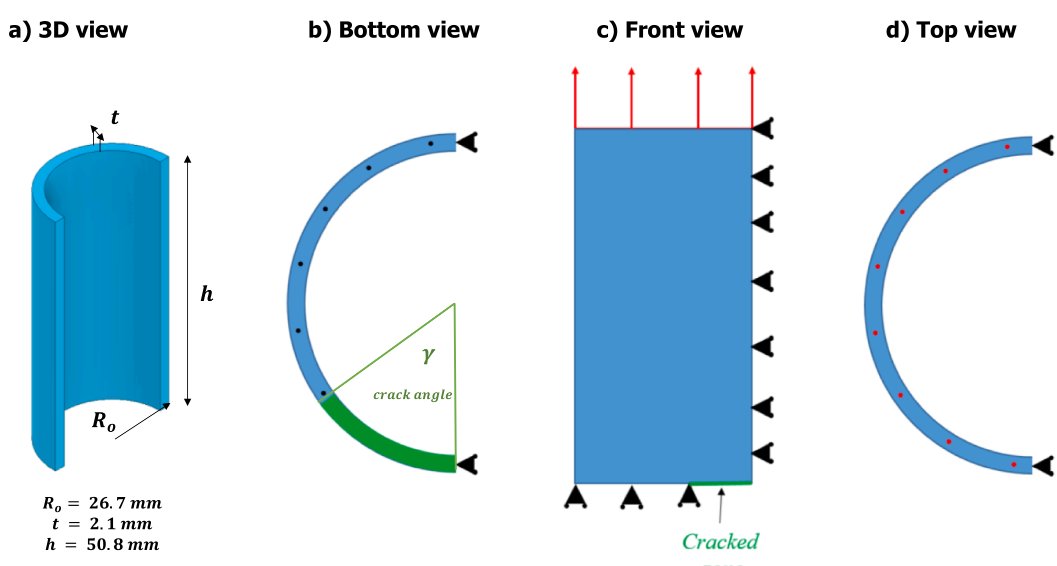

Fig. 6. FEA model, geometry and boundary conditions. (a) 3D view, (b) bottom view, (c) front view and (d) top view. The black points indicate boundary condition applied and the red points applied load. (For interpretation of the references to colour in this figure legend, the reader is referred to the web version of this article.)

Table 3
Parameters for the combined hardening model of the material [39].

$C(MPa)$	D	$Q(MPa)$	b
528,000	300	87	9

node release method was used to model fatigue crack growth assuming a constant fatigue crack growth rate [39,46] due to its potential and simplicity. In this way, every-three loading cycle's, through-thickness nodes were released thus causing the crack growth [40]. This method was implemented in ABAQUS employing a user-subroutine. The range of the crack lengths simulated was from 5 to 60 degrees (in terms of the crack angle defined in Fig. 6). Through-thickness nodes were released as radial straight lines and hence, modelling a straight crack front.

5. Methodologies for SIF determination

5.1. SIF calculation from experimental data

SIF were inferred for the maximum cycle load, thus, the experimentally measured crack tip displacement fields under maximum load were employed. 3D-DIC data provides the three dimensional displacement field as well as the spatial coordinates on the analysed surface. The first step is to calculate Frenet-Serret unitary vectors defined in Section 2 that depend on the coordinates and the crack growth and crack opening directions. In this particular case, the crack growth direction (ξ) coincides with the circumferential direction and the crack opening direction (η) is the axial direction. These parametrisation directions were calculated through the surface coordinates measured with 3D-DIC. Note that in this particular case, the geometrical transformation coincides

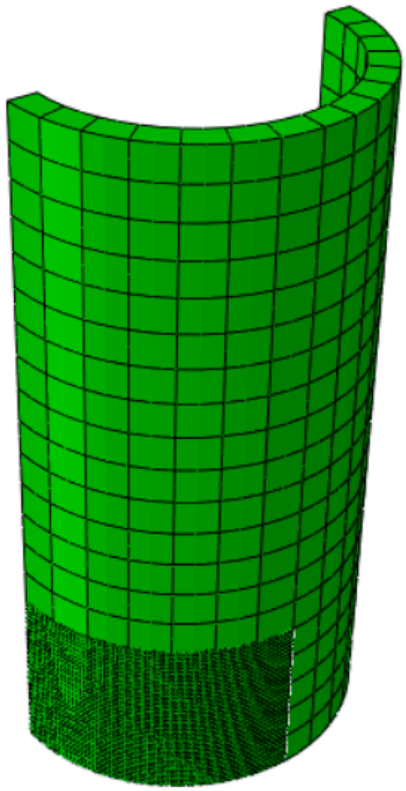

Fig. 7. Computational domain. Coarse and refined meshes.

with a transformation to cylindrical coordinates. Thus, once parametrisation directions have been defined, Frenet-Serret vectors are calculated at each point on the surface using equations (5)–(7). Spatial derivatives were addressed by a finite difference approach. The first order central derivative was employed to improve the calculus accuracy. By combining Frenet-Serret vectors and the experimentally measured displacement field, the transformed displacement field was calculated. Curve coordinates was calculated from equations (8) and (9) by employing numerical integration. Fig. 8 shows both tangential and binormal displacement maps onto the unwrapped surface for a crack length of 26.1 mm (0.31 in terms of the normalised crack length. The normalised crack length was defined as the ratio between the crack angle (γ angle defined in Sections 2 and 4) and the half circumference angle (π radians).

To estimate the crack tip characterising parameters, the Multi-Point Over-Deterministic method developed by Sanford and Dally was employed [47]. An annular collection as shown in Fig. 9 was used for fitting in order to avoid the surrounding crack tip plasticity area where linear elastic fracture mechanics parameters do not govern the singularity. The inner radius was chosen to be higher than that estimated via Dugdale plastic radius approximation [48], which provides an overestimation of the plastic radius and hence avoids partial inclusion of nonlinear data near the crack tip. The outer radius was initially selected according to Nurse et al [49] criterion as a fraction of the crack length (0.4). However, slight and hence not significant differences were found in terms of inferred crack tip parameters for higher values of the outer radius. A linear distribution between the mesh points was chosen for simplicity. No significant differences were found in relation to other high order polynomial mathematical distributions. Once data has been extracted at the mesh points (binormal and tangential displacement) and its curve coordinates, crack tip parameters were calculated by solving a linear equation system. Williams' model was fitted by employing 2, 3 and 4 terms of the expansion series being 4 terms the value where the model becomes stable for all analysed data. In other words, obtained crack tip parameters when higher order terms are included do not change their values regarding those obtained using 4 series terms. The crack tip location plays an important role during fitting process since the mesh points coordinates must be referred to the crack tip. To avoid this problem, a search region was defined by enclosing a confidence region surrounding the crack tip [24] and the fitting quality was assessed at each point using equation (15). Thus, the point of higher fitting correlation coefficient and hence minimum error should correspond to the crack tip location [50,51]. In this point, the coefficients that describe the crack tip field and the SIFs were finally calculated.

$$F^{exp} = \sqrt{\left\|\frac{u_T^{th} - u_T^{exp}}{u_T^{th}}\right\|^2 + \left\|\frac{u_B^{th} - u_B^{exp}}{u_B^{th}}\right\|^2} \tag{15}$$

In equation (15), double vertical bars note the two-norm operator and superscripts *exp* and *th* refer to experimental and theoretical displacement data, respectively.

5.2. SIF determination from numerical data

Opening mode SIFs were determined at the maximum loading cycle for different crack lengths from numerically determined fields. Opening mode SIFs were calculated by analysing both stress and displacement profiles ahead and behind the crack tip, respectively. Thus, two values were obtained to check the measurement goodness. From the axial displacement along a horizontal line (tangential direction) behind the

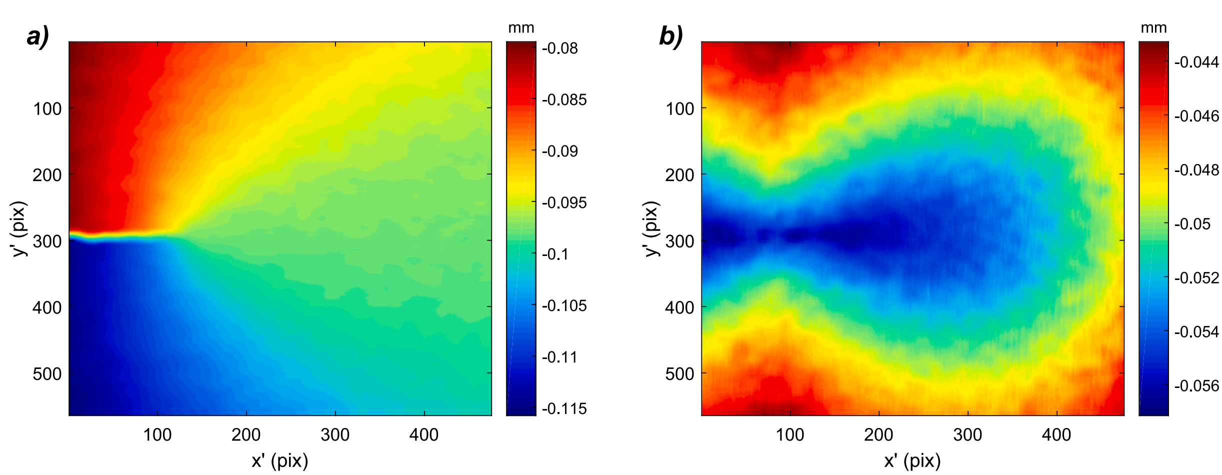

Fig. 8. Displacement fields around the crack tip in terms of binormal and tangential directions at the maximum load of 20 kN for a crack length of 26.1 mm (normalised crack length $\gamma/\pi = 0.31$). (a) Binormal and (b) tangential components.

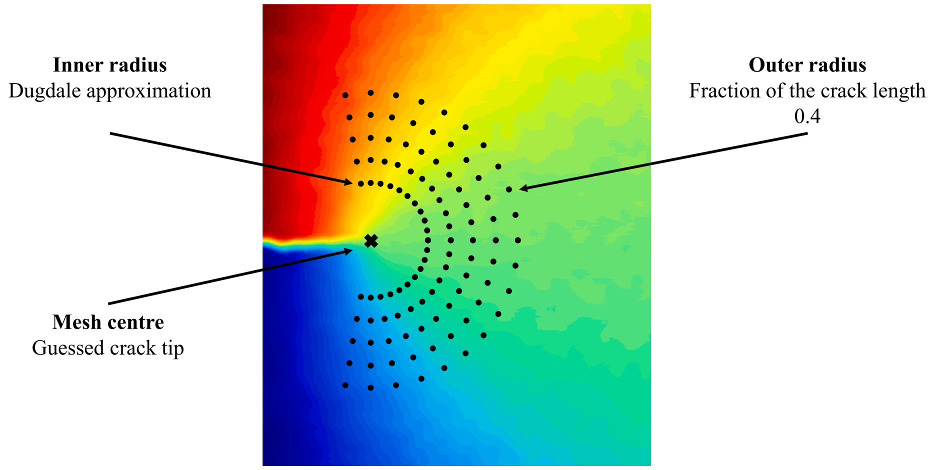

Fig. 9. Annular shape mesh for collecting experimental fitting data over an axial component map.

crack tip, K_I was determined by fitting those data to 2-terms Williams' equation ($\theta = 180^{\circ}$) as shown in equation (16).

$$u_{axial} = \frac{K_I}{2G}\sqrt{\frac{r}{2\pi}}(\kappa+1) + u_{0,axial} \tag{16}$$

Analogously to that exposed above, K_I was also obtained from the axial stress ahead of the crack tip. In this case, 2-terms Williams' stress equation ($\theta = 0$) and including a constant term that models an axial non-singular stress is given by equation (17).

$$\sigma_{axial} = \frac{K_I}{\sqrt{2\pi r}} + \sigma_{0,axial} \tag{17}$$

To avoid the inclusion of plastic data, both profiles were filtered by removing points that exceed 0.2 % Yield Stress using the von Mises criterion. An example of both the axial stress and axial displacement profiles for a crack length of 45 degrees (0.25 in terms of the normalised crack length) are shown in Fig. 10.

In both cases, to provide a fitting goodness value, the relative error between numerical and theoretical fitted data (described in the following Section 5.3) was computed. The two fitting quality parameters are:

$$F^{num}_{disp} = \left\|\frac{u^{th}_{axial} - u^{num}_{axial}}{u^{th}_{axial}}\right\| \tag{18}$$

$$F^{num}_{stress} = \left\|\frac{\sigma^{th}_{axial} - \sigma^{num}_{axial}}{\sigma^{th}_{axial}}\right\| \tag{19}$$

Where F^{num}_{disp} and F^{num}_{stress} are fitting quality parameters for the displacement and the stress numerical data, respectively, and superscripts *th* and *num* denote the theoretical and numerical data nature.

5.3. Theoretical determination of the stress intensity factor

To support also experimental and numerical stress intensity factors, a theoretical value of the stress intensity factor was computed by employing Tada's equation [52] based on Sanders' results [53,54].

$$K_I = \frac{P}{2\pi R t}\sqrt{R}\left(\frac{\sqrt{2}}{\left(\frac{t}{R\sqrt{12(1-\nu^2)}}\right)^{\frac{1}{2}}}\right)^{\frac{1}{2}}\left(\gamma + \frac{1-\gamma \bullet \cos\gamma}{2\cot\gamma + \sqrt{2}\cot\left(\frac{\pi-\gamma}{\sqrt{2}}\right)}\right) \tag{20}$$

Where P is the remote applied axial load, R is the pipe mean radius, t is the wall thickness, ν is Poisson's ratio and γ is crack angle.

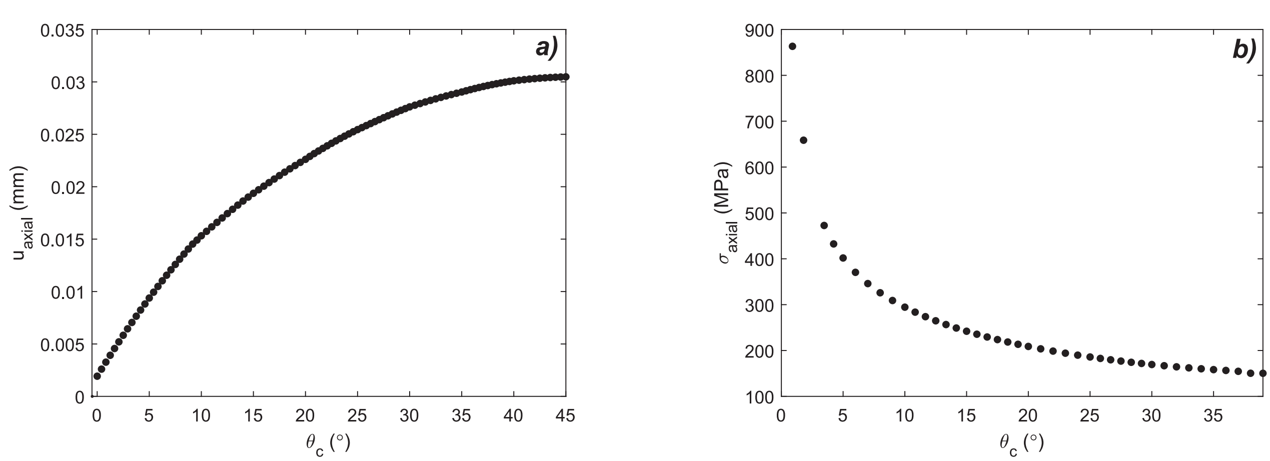

Fig. 10. (a) Axial displacement profile at $\theta = 180^{\circ}$ (behind the crack tip) and (b) Axial stress profile at $\theta = 0^{\circ}$ (ahead of the crack tip). Origin at the crack tip and θ_c is the tangential angle in the cylinder system.

6. Results and discussion

6.1. Plane stress hypothesis verification

One of the initial assumptions for extending original crack tip field models to the analysis of 3D nonplanar surfaces is the plane stress hypothesis (radial stress zero). From experimental data, this hypothesis cannot be directly demonstrated since only surface data can be acquired and through-thickness displacement gradients are required to compute the radial stress. However, from numerical analysis, this hypothesis can be checked simply. Fig. 11 shows radial stress profiles for a normalised crack length of 0.25. As shown, radial stress at the surface is almost zero (lower than 0.5 MPa). This close to zero stress value might be due to a residual numerical computation. Nonetheless, the maximum value of that numerical residual stress is 0.4 % of the remote applied maximum load and it can be assumed as negligible. Higher errors were found at $z_c = 0$ profile (crack growth direction) and close to the crack tip (at origin in Fig. 11); however, this fact seems meaningful due to crack tip stress triaxiality. A value around 250 MPa was found just at the crack tip and then immediately descends to almost zero. Therefore, a pure plane stress state exists at the cylinder surface.

6.2. Single-parameter comparison using stress intensity factors

Fig. 12a shows theoretical, numerical and experimental stress intensity factors as a function of the normalised crack length. The increase of crack length produces an increase of K_I, as could be expected. As shown, all the stress intensity factors show a high level of agreement with the theoretical values. To quantify the agreement between both data, the average relative error between these numerical and experimental values were computed. These errors were 6.4 % for the experimental value employing 2 terms in Williams' series, 4.7 % for the experimental value employing 3 terms in Williams' series, 3.4 % for the experimental value employing 4 terms in Williams' series, 4.0 % for the numerical from displacement value and 4.3 % for the numerical from the stress value. A higher deviation was found for higher cracks, however, this does not imply that the proposed methodology is limited to a certain normalised crack length since in the work by Camacho-Reyes *et al.* [24] is described that the methodology is valid for all range of normalised crack lengths and the major limitation lies in the existence of a plastic zone. In fact, results reported in [24] agree with SSY limits ($\gamma/\pi \approx < 0.7$) provided by ASTM E647 00 [55]. For experimental stress intensity factors, the normalised 95 % confidence intervals were calculated in order to provide a measurement accuracy value. At shorter crack lengths, a higher dispersion was found (0.2). It is believed that this high dispersion might be attributed to the effect of residual stresses induced during the notch manufacturing process. However, this value is rapidly reduced to 0.01 as the crack grow. Thus, the mean value for the different crack lengths and Williams' terms (2, 3 and 4) is 0.03 ($K_I \pm 3$ %). Fig. 12b shows the computed stress intensity factors (numerical and experimental) as a function of the nominal or theoretical values together with 5 % tolerance lines. Again, the high level of agreement between both data is reported in this graph.

In addition, to assess the fitting quality, the correlation between the theoretical-fitted data and the experimental or numerical data are presented in terms of the fitting quality parameters described in above section (equations (15), (18) and (19)). Thus, the average value of these parameters is 0.05 % for the three set of experimental data (2, 3 and 4 Williams' series terms), 0.35 % for the numerical displacement data and 3 % for the numerical stress data.

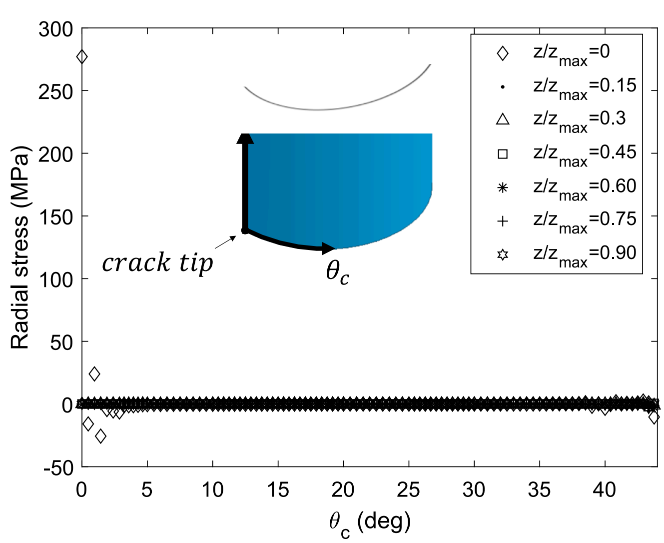

Fig. 11. Radial stress for a normalised crack length of 0.25. (a) Profiles for different z distances (axial coordinate). Origin at crack tip.

6.3. Full-field comparison between FEA and DIC data using image decomposition

In the above section, a comparison between stress intensity factors has been performed. However, to support the proposed methodology, a comprehensive comparative has been done via comparing experimentally and numerically inferred displacement fields. This allows checking the validity of the proposed methodology beyond comparing only one crack tip parameter as the stress intensity factor. A problem for the direct comparison lies in the resolution of both displacement fields that are not the same and hence, complicates this analysis. The Image Decomposition technique described in Section 2 has been employed to avoid this inconvenience. This technique allows fields to be compared without dependence on either length or orientation of the domain. Thus, three displacement fields (considering the in-unwrapped plane components) at three different normalised crack lengths (0.16, 0.27 and 0.32) were compared. As example, the numerical and experimental displacement field components on the cylinder surface for a normalised crack length of 0.27 are shown in Fig. 13. It is important to note that only the upper part of the field has been compared due to the symmetry condition with respect to the mid radial-tangential plane.

In this work, each displacement map have been decomposed into 20 shape descriptors which is enough to obtain a correlation coefficient higher than 0.97 between the original maps and those reconstructed.

In Fig. 14, a scattered plot is presented in which the feature vector obtained by FEA against the one obtained experimentally is shown. Hence, similarity between both vectors is evaluated by the closeness to a 45 degrees line, displayed as a green line. In this plot, it is also evaluated the uncertainty of the decomposition procedure which is calculated as the Root Mean Square (RMS) value of the difference between original and reconstructed displacement map and it is presented by the red dashed lines at both sides of the 45 degree line. As observed, most of data of the feature vectors lie within the uncertainty bands that show the good agreement between data sets for all the crack lengths and for the tangential and binormal components. The correlation coefficient between data sets for displacement maps and for each crack length is also calculated and a correlation higher than 0.98 between experimental and numerical results is always obtained. This value shows the high level of agreement between both numerical and experimental maps.

Moreover, it is possible to achieve a percentage of difference by relating the norm of the difference of feature vectors and the maximum value obtained in the displacement map. Fig. 15 shows the difference in percentage between the experimental and numerical results along the normalised crack length. As observed, a maximum difference of 12.6 % is obtained at the minimum crack length (0.16 in terms of the normalised crack length) for the tangential displacement map; for the rest of crack lengths is below 9 %. This fact also reinforces the high level of agreement between both experimental and numerical maps.

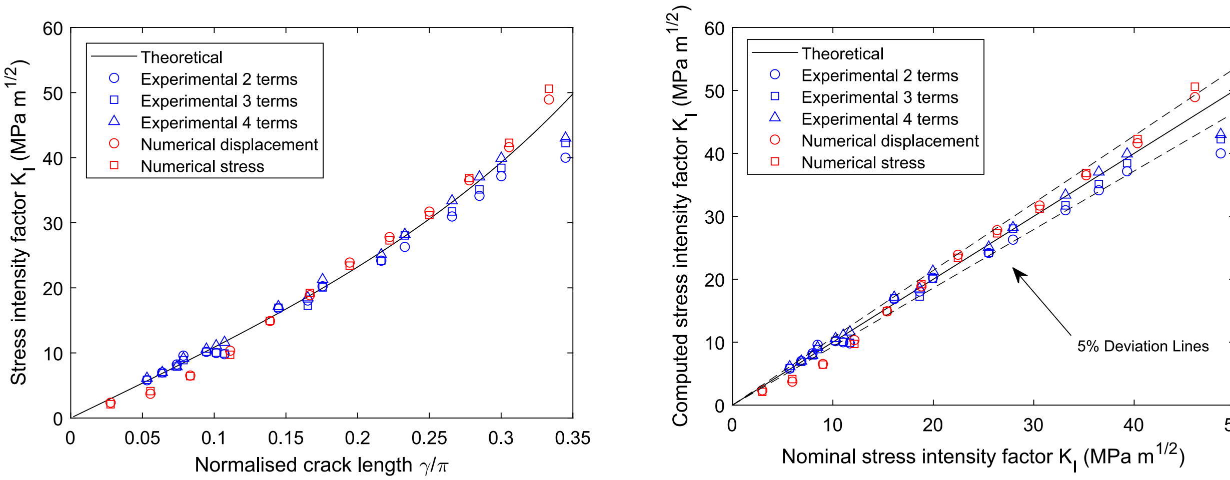

Fig. 12. (a) Computed theoretical, experimental and numerical stress intensity factors versus normalised crack length and (b) numerical and experimental computed stress intensity factors vs nominal stress intensity factors.

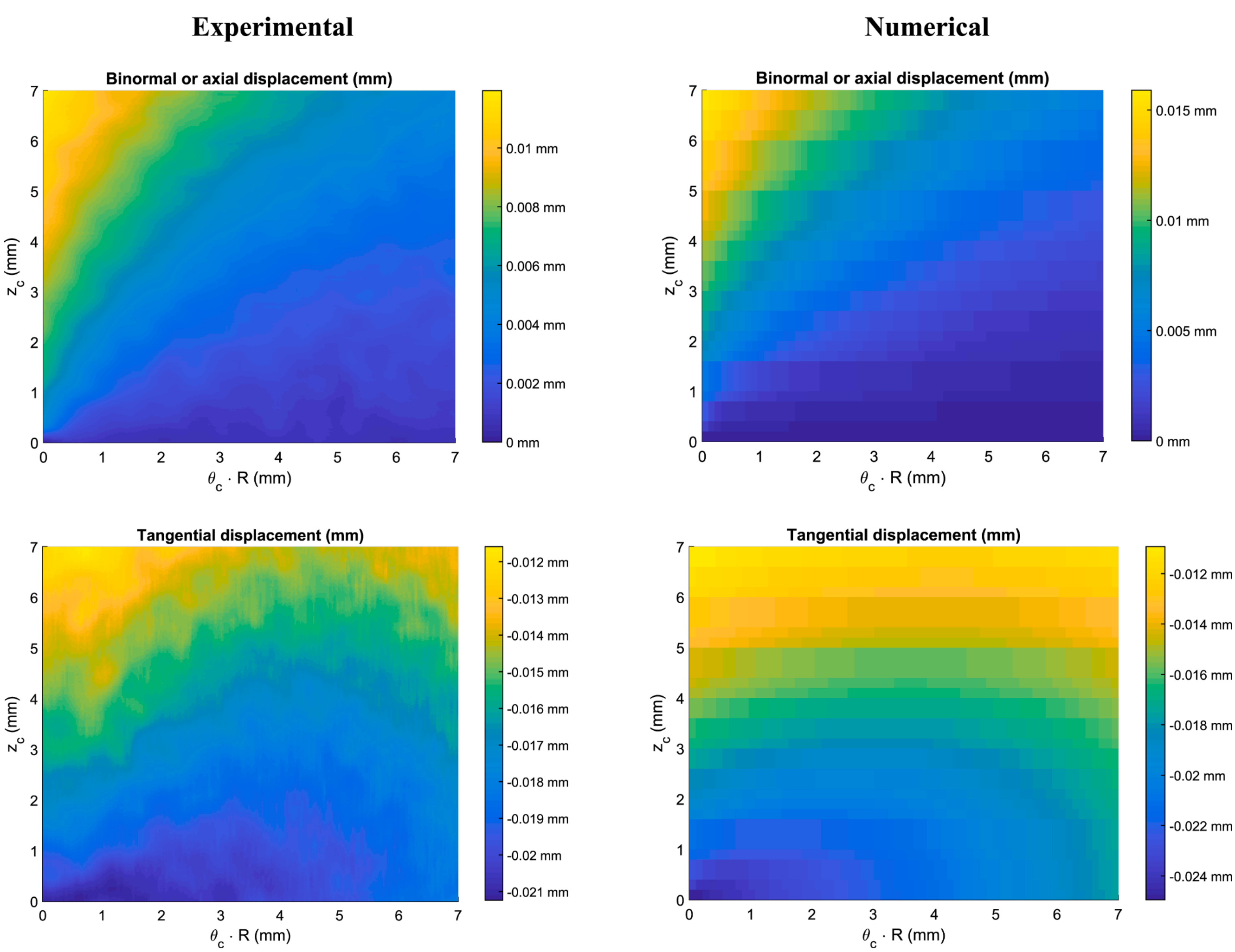

Fig. 13. Example of numerical and experimental displacement field components maps for Image Decomposition technique. Origin at the crack tip. Maps for a normalised crack length of 0.27.

7. Conclusions

In this work, a numerical and experimental study about characterising crack tip fields on non-planar and developable surfaces under plane stress conditions has been performed. Results show a high level of agreement for both stress intensity factors and crack tip displacement fields. As previously described, the key to the success of this approach is due to the plane stress state occurring at the element as well as the fact

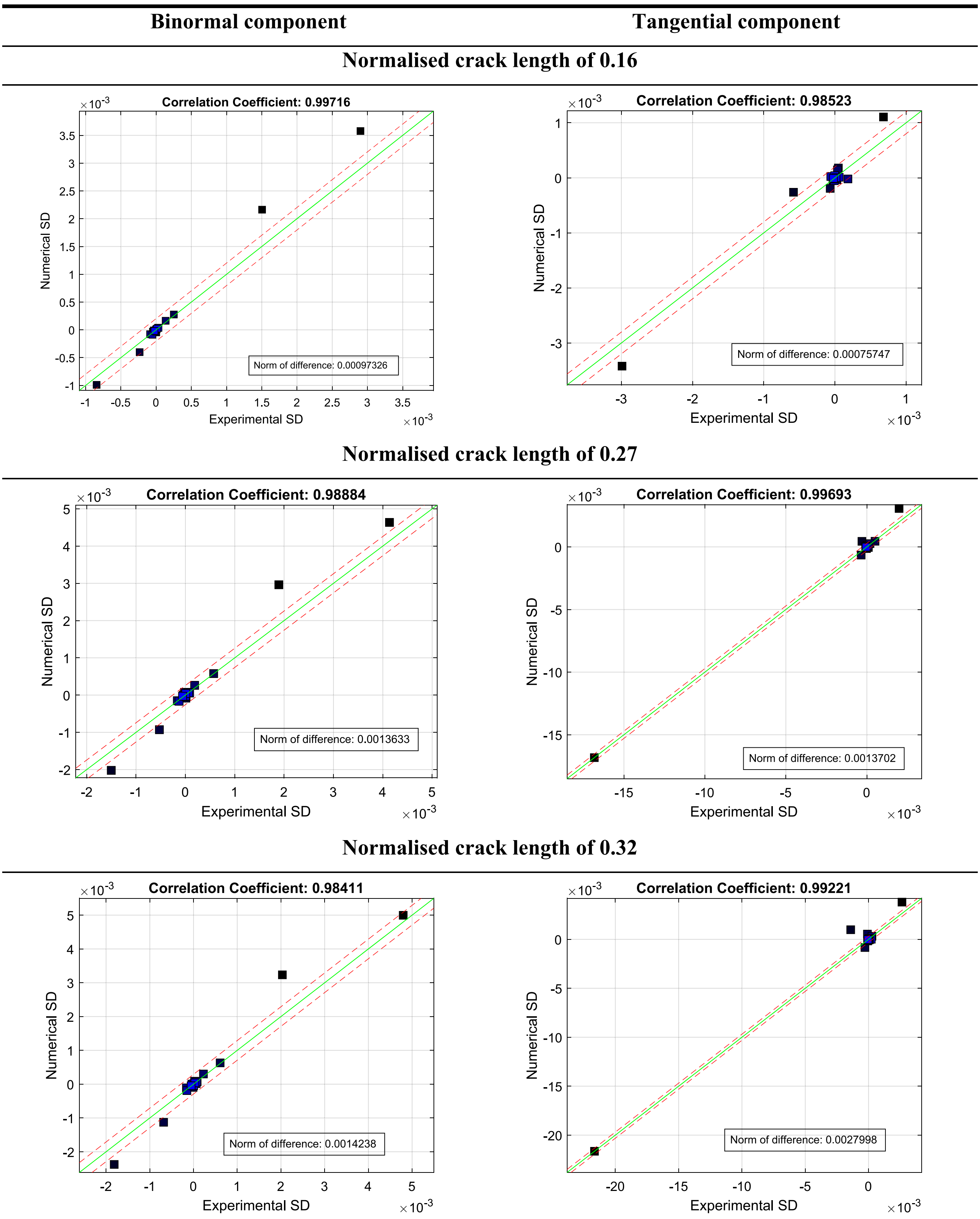

Fig. 14. Numerical vs experimental maps, left binormal and right tangential components, shape descriptors for different crack lengths, 0.16, 0.27 and 0.32.

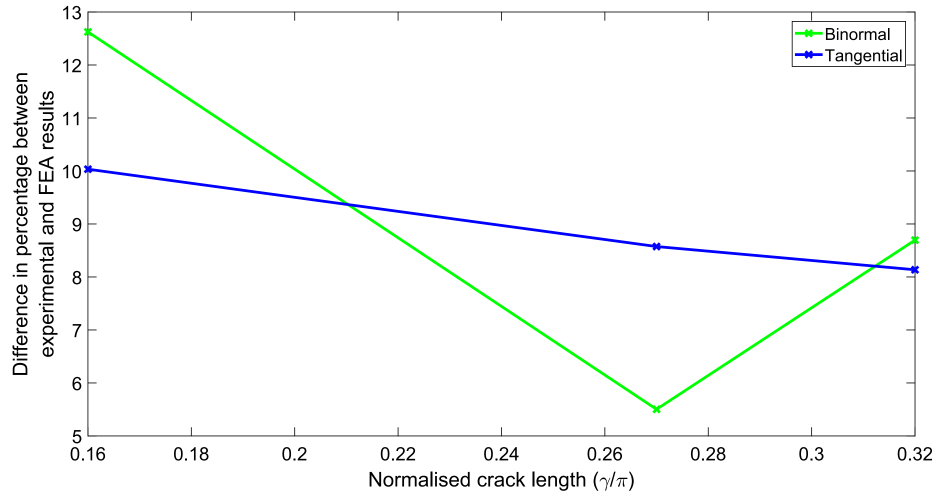

Fig. 15. Difference in percentage between maximum values of experimental and FEA results for different crack lengths (0.16, 0.27 and 0.32 in terms of the normalised crack length).

that it can be unwrapped without distortion and hence stablishing a direct analogy with original flat crack tip field models. The main attraction of the exposed methodology lies in the possible analysis of non-flat, zero Gaussian curvature cracked bodies under plane stress conditions for fatigue or fracture assessment from a theoretical–experimental approach. Some direct potential applications are, the fatigue analysis of thin-wall curved components through the experimentally determination of ΔK, ΔK_{eff} or even ΔJ, which are sometimes calculated approximately due to the curvature effect, as well as plasticity-induced crack tip shielding assessment via advanced crack tip field models providing effective fatigue crack driving forces. Beyond fatigue applications, this methodology can be used to support and validate complex geometry problems by providing experimental data (i.e. some crack tip parameters) on the specimen surface as verification parameters. Although the exposed methodology has been validated under pure mode I, an extension to mixed-mode loading would only require some minor geometrical modifications. Thus, complex geometries under not only uniaxial loading conditions can be experimentally addressed and hence clarifying some fatigue and fracture issues related to mixed-mode fatigue crack growth.

Interest competition

The authors declare that they have no known competing financial interests or personal relationships that could have appeared to influence the work reported in this paper.

Authors contribution

F.A. Diaz conceived the original idea. A. Camacho-Reyes performed the experimental work and J.M. Vasco-Olmo its supervision. A Camacho-Reyes perfomed the numerical work and F.V. Antunes its supervision. L.A. Felipe-Sese performed the comparison between data using the comparison-technique described. All authors worked on the analysis, interpretation and discussion of the results, where the most critical feedback was provided by F.A. Diaz and F.V. Antunes. A. Camacho-Reyes took the lead in writing the original version of the manuscript and the rest of authors contributed to its final version through their critical comments, editions and reviews. All authors agree on the order in which their names are listed in the manuscript.

Declaration of Competing Interest

The authors declare that they have no known competing financial interests or personal relationships that could have appeared to influence the work reported in this paper.

Data availability

The data that support the findings of this study are available from the corresponding author upon reasonable request

Acknowledgements

The authors want to acknowledge the financial support from Junta de Andalucía through the research project "1380786" funded by the program "Proyectos de I + D + i en el Marco del Programa Operativo FEDER Andalucía 2014-2020. Convocatoria 2020" and to EDUJA Escuela de Doctorado de la Universidad de Jaén (Jaén University Doctoral School) for the mobility grant "Ayudas de la EDUJA para Estancias Destinadas a la Obtención de la Mención Internacional en el Título de Doctor" without this work could not be performed.

This research is also sponsored by Portuguese National Funds through FCT – Fundação para a Ciência e a Tecnologia –, under the project UIDB/00285/2020.

References

[1] M.A. Sutton, J.J. Orteu, H.W. Schreier, Image Correlation for Shape, Motion and Deformation Measurements, Springer US, New York, 2009, doi: 10.1007/978-0-387-78747-3.
[2] W. Thomson, K. Lord, On the thermoelastic, thermomagnetic and pyro-electric properties of matters, Phil. Mag. 5 (1878) 4–27.
[3] D. Brewster, On the communication of the structure of doubly refracting crystals to glass, muriate of soda, flour spar and other substances by mechanical compression and dilatation, Phil. Mag. 106 (1816) 156–178.
[4] H.M. Westergaard, Bearing pressures and cracks, J. Appl. Mech. 61 (1939) 49–53.
[5] G.R. Irwin, Analysis of stresses and strains near the end of a crack traversing plate, J. Appl. Mech. 24 (1957) 361–370.
[6] M.L. Williams, On the stress distribution at the base of a stationary crack, J. Appl. Mech. 24 (1957) 109–114.
[7] S. Pommier, R. Hamam, Incremental model for fatigue crack growth based on a displacement partitioning hypothesis of mode I elastic-plastic displacement fields, Fatigue Fract. Eng. Mater. Struct. 30 (2007) 582–598, https://doi.org/10.1111/j.1460-2695.2007.01128.x.
[8] C.J. Christopher, M.N. James, E.A. Patterson, K.F. Tee, Towards a new model of crack tip stress fields, Int. J. Fract. 148 (2007) 361–371, https://doi.org/10.1007/s10704-008-9209-3.
[9] C.J. Christopher, M.N. James, E.A. Patterson, K.F. Tee, A quantitative evaluation of fatigue crack shielding forces using photoelasticity, Eng. Fract. Mech. 75 (2008) 4190–4199, https://doi.org/10.1016/j.engfracmech.2008.03.013.
[10] M.N. James, C.J. Christopher, Y.W. Lu, E.A. Patterson, Local crack plasticity and its influences on the global elastic stress field, Int. J. Fatigue 46 (2013) 4–15, https://doi.org/10.1016/j.ijfatigue.2012.04.015.

[11] B. Yang, J.M. Vasco-Olmo, F.A. Díaz, M.N. James, A more effective rationalisation of fatigue crack growth rate data for various specimen geometries and stress ratios using the CJP model, Int. J. Fatigue 114 (2018) 189–197, https://doi.org/10.1016/j.ijfatigue.2018.05.027.
[12] D. Nowell, S.C. Nowell, A comparison of recent models for fatigue crack tip deformation, Theor. Appl. Fract. Mech. 103 (2019) 6, https://doi.org/10.1016/j.tafmec.2019.102299.
[13] F.A. Diaz, J.M. Vasco-Olmo, E. Lopez-Alba, L. Felipe-Sese, A.J. Molina-Viedma, D. Nowell, Experimental evaluation of effective stress intensity factor using thermoelastic stress analysis and digital image correlation, Int. J. Fatigue 135 (2020) 10, https://doi.org/10.1016/j.ijfatigue.2020.105567.
[14] J.M. Vasco-Olmo, M.N. James, C.J. Christopher, E.A. Patterson, F.A. Diaz, Assessment of crack tip plastic zone size and shape and its influence on crack tip shielding, Fatigue Fract. Eng. Mater. Struct. 39 (2016) 969–981, https://doi.org/10.1111/ffe.12436.
[15] B. Yang, Z. Wei, F.A. Díaz, Z. Liao, M.N. James, New algorithm for optimised fitting of DIC data to crack tip plastic zone using the CJP model, Theor. Appl. Fract. Mech. 113 (2021), 102950, https://doi.org/10.1016/J.TAFMEC.2021.102950.
[16] P. Lopez-Crespo, A. Shterenlikht, E.A. Patterson, J.R. Yates, P.J. Withers, The stress intensity of mixed mode cracks determined by digital image correlation, J. Strain Anal. Eng. Des. 43 (2008) 769–780, https://doi.org/10.1243/03093247jsa419.
[17] J.R. Yates, M. Zanganeh, Y.H. Tai, Quantifying crack tip displacement fields with DIC, Eng. Fract. Mech. 77 (2010) 2063–2076, https://doi.org/10.1016/j.engfracmech.2010.03.025.
[18] P. Lopez-Crespo, B. Moreno, A. Garcia-Gonzalez, J. Zapatero, A. Lopez-Moreno, Study of short cracks under biaxial fatigue, Frat Ed Integrità Strutt 8 (2014) 244–251, https://doi.org/10.3221/IGF-ESIS.30.31.
[19] M. Mokhtari, P. Lopez-Crespo, B. Moreno, M. Zanganeh, Some experimental observations of crack-tip mechanics with displacement data, Frat Ed Integrità Strutt 9 (2015) 143–150, https://doi.org/10.3221/IGF-ESIS.33.18.
[20] P. Lopez-Crespo, A. Garcia-Gonzalez, B. Moreno, A. Lopez-Moreno, J. Zapatero, Some observations on short fatigue cracks under biaxial fatigue, Theor. Appl. Fract. Mech. 80 (2015) 96–103, https://doi.org/10.1016/J.TAFMEC.2015.05.004.
[21] P. Lopez-Crespo, B. Moreno, A. Lopez-Moreno, J. Zapatero, Study of crack orientation and fatigue life prediction in biaxial fatigue with critical plane models, Eng. Fract. Mech. 136 (2015) 115–130, https://doi.org/10.1016/J.ENGFRACMECH.2015.01.020.
[22] M. Mokhtarishirazabad, P. Lopez-Crespo, B. Moreno, A. Lopez-Moreno, M. Zanganeh, Optical and analytical investigation of overloads in biaxial fatigue cracks, Int. J. Fatigue 100 (2017) 583–590, https://doi.org/10.1016/j.ijfatigue.2016.12.035.
[23] M. Vormwald, Y. Hos, J.L.F. Freire, G.L.G. Gonzales, J.G. Diaz, Crack tip displacement fields measured by digital image correlation for evaluating variable mode-mixity during fatigue crack growth, Int. J. Fatigue 115 (2018) 53–66, https://doi.org/10.1016/j.ijfatigue.2018.04.030.
[24] A. Camacho-Reyes, J.M. Vasco-Olmo, M.N. James, F.A. Diaz, Characterization of non-planar crack tip displacement fields using a differential geometry approach in combination with 3D digital image correlation, Fatigue Fract. Eng. Mater. Struct. (2022), https://doi.org/10.1111/ffe.13686.
[25] G. Lampeas, V. Pasialis, X. Lin, E.A. Patterson, On the validation of solid mechanics models using optical measurements and data decomposition, Simul. Model. Pract. Theory 52 (2015) 92–107, https://doi.org/10.1016/j.simpat.2014.12.006.
[26] C. Sebastian, E. Hack, E. Patterson, An approach to the validation of computational solid mechanics models for strain analysis, J. Strain Anal. Eng. Des. 48 (2013) 36–47, https://doi.org/10.1177/0309324712453409.
[27] W. Wang, J.E. Mottershead, T. Siebert, A. Pipino, Frequency response functions of shape features from full-field vibration measurements using digital image correlation, Mech. Syst. Sig. Process. 28 (2012) 333–347, https://doi.org/10.1016/J.YMSSP.2011.11.023.
[28] S. Kobayashi, Differential geometry of curves and surfaces, Singapore: Springer Singapore (2010), https://doi.org/10.1007/978-981-15-1739-6.
[29] E. Hack, G. Lampeas, E.A. Patterson, An evaluation of a protocol for the validation of computational solid mechanics models, J. Strain Anal. Eng. Des. 51 (2016) 5–13, https://doi.org/10.1177/0309324715616017.
[30] C. Sebastian, E. Hack, E. Patterson, An approach to the validation of computational solid mechanics models for strain analysis, J. Strain Anal. Eng. Des. 48 (2012) 36–47, https://doi.org/10.1177/0309324712453409.
[31] R. Mukundan, S.H. Ong, P.A. Lee, Image analysis by Tchebichef moments, IEEE Trans. Image Process. 10 (2001) 1357–1364, https://doi.org/10.1109/83.941859.
[32] W. Wang, J.E. Mottershead, A. Ihle, T. Siebert, H.R. Schubach, Finite element model updating from full-field vibration measurement using digital image correlation, J. Sound Vib. 330 (2011) 1599–1620, https://doi.org/10.1016/j.jsv.2010.10.036.
[33] R.L. Burguete, G. Lampeas, J.E. Mottershead, E.A. Patterson, A. Pipino, T. Siebert, et al., Analysis of displacement fields from a high-speed impact using shape descriptors, J. Strain Anal. Eng. Des. 49 (2014) 212–223, https://doi.org/10.1177/0309324713498074.
[34] ASTM. E 606 - 92: Standard Practice for Strain-Controlled Fatigue Testing, Annu B ASTM Stand 1103 1998;E-606-92.
[35] S. Kalnaus, F. Fan, Y. Jiang, A.K. Vasudevan, An experimental investigation of fatigue crack growth of stainless steel 304L, Int. J. Fatigue 31 (2009) 840–849, https://doi.org/10.1016/J.IJFATIGUE.2008.11.004.
[36] www.correlatedsolutions.com, n.d.
[37] E. Voce, The relationship between stress and strain for homogeneous deformation, J. Inst. Met. 74 (1948) 537–562.
[38] J.L. Chaboche, A review of some plasticity and viscoplasticity constitutive theories, Int. J. Plast. 24 (2008) 1642–1693, https://doi.org/10.1016/J.IJPLAS.2008.03.009.
[39] F.V. Antunes, M.S.C. Ferreira, R. Branco, P. Prates, C. Gardin, C. Sarrazin-Baudoux, Fatigue crack growth versus plastic CTOD in the 304L stainless steel, Eng. Fract. Mech. 214 (2019) 487–503, https://doi.org/10.1016/j.engfracmech.2019.04.013.
[40] D. Camas, J. Garcia-Manrique, F.V. Antunes, A. Gonzalez-Herrera, Three-dimensional fatigue crack closure numerical modelling: crack growth scheme, Theor. Appl. Fract. Mech. 108 (2020), 102623, https://doi.org/10.1016/j.tafmec.2020.102623.
[41] M.F. Borges, P. Lopez-Crespo, F.V. Antunes, B. Moreno, P. Prates, D. Camas, et al., Fatigue crack propagation analysis in 2024–T351 aluminium alloy using nonlinear parameters, Int. J. Fatigue 153 (2021), 106478, https://doi.org/10.1016/J.IJFATIGUE.2021.106478.
[42] L. Yao-Chen, The finite element method by employing the singular element with concordant displacement at the crack tip, Eng. Fract. Mech. 19 (1984) 959–972, https://doi.org/10.1016/0013-7944(84)90173-5.
[43] A. García-Collado, J.M. Vasco-Olmo, F.A. Díaz, Numerical analysis of plasticity induced crack closure based on an irreversible cohesive zone model, Theor. Appl. Fract. Mech. 89 (2017) 52–62, https://doi.org/10.1016/J.TAFMEC.2017.01.006.
[44] L. Min, X. Hu, W. Yao, T.Q. Bui, P. Zhang, On realizing specific failure initiation criteria in the phase field model, Comput. Methods Appl. Mech. Eng. 394 (2022), 114881, https://doi.org/10.1016/J.CMA.2022.114881.
[45] P. Zhang, S. Tan, X. Hu, W. Yao, X. Zhuang, A double-phase field model for multiple failures in composites, Compos. Struct. 293 (2022), 115730, https://doi.org/10.1016/J.COMPSTRUCT.2022.115730.
[46] J.H. Hwang, Y.J. Kim, J.W. Kim, Load interaction effect on fatigue crack growth in through-wall cracked pipes under large scale yielding: experimental and numerical investigation, Int. J. Mech. Sci. 211 (2021), 106761, https://doi.org/10.1016/j.ijmecsci.2021.106761.
[47] R.J. Sanford, J.W. Dally, A general method for determining mixed-mode stress intensity factors from isochromatic fringe patterns, Eng. Fract. Mech. 621 (1979) 621–633.
[48] D.S. Dugdale, Yielding of steel sheets containing slits, J. Mech. Phys. Solids 8 (1960) 100–104, https://doi.org/10.1016/0022-5096(60)90013-2.
[49] A.D. Nurse, E.A. Patterson, Experimental determination of stress intensity factors for cracks in turbine disks, Fatigue Fract. Eng. Mater. Struct. 16 (1993) 315–325, https://doi.org/10.1111/j.1460-2695.1993.tb00089.x.
[50] S. Yoneyama, Y. Morimoto, M. Takashi, Automatic evaluation of mixed-mode stress intensity factors utilizing digital image correlation, Strain 42 (2006) 21–29, https://doi.org/10.1111/j.1475-1305.2006.00246.x.
[51] M. Zanganeh, P. Lopez-Crespo, Y.H. Tai, J.R. Yates, Locating the crack tip using displacement field data: a comparative study, Strain 49 (2013) 102–115, https://doi.org/10.1111/str.12017.
[52] H. Tada, P.C. Paris, G.R. Irwin, The Stress Analysis of Cracks Handbook, third ed., ASME Press, New York, 2000, doi: 10.1115/1.801535.
[53] J.L. Sanders, Circumferential through-cracks in cylindrical-shells under tension, J. Appl. Mech. ASME 49 (1982) 103–107, https://doi.org/10.1115/1.3161948.
[54] J.L. Sanders, Analysis of circular cylindrical-shells, J. Appl. Mech. ASME 50 (1983) 1165–1170, https://doi.org/10.1115/1.3167198.
[55] ASTM. E 647 - 00: Standard Test Method for Measurement of Fatigue Crack Growth Rates, Annu B ASTM Stand 1103 2000.